Nanopatterned optical and magnetic $La_{0.6}Ca_{0.4}MnO_3$ arrays: Synthesis, fabrication, and properties

Ming-Chung Wu, Chih-Min Chuang, Jhih-Fong Lin, and Yu-Ching Huang
Department of Materials Science and Engineering, National Taiwan University, Taipei 106-17, Taiwan
Yang-Fang Chen
Department of Physics, National Taiwan University, Taipei 106-17, Taiwan
Wei-Fang Su[a)]
Department of Materials Science and Engineering, National Taiwan University, Taipei 106-17, Taiwan

(Received 4 April 2008; accepted 8 October 2008)

We have fabricated $La_{0.6}Ca_{0.4}MnO_3$ periodic arrays exhibiting tunable optical properties and magnetic properties using nontoxic and environmentally friendly electron beam resist made from $La_{0.6}Ca_{0.4}MnO_3$ sol-gel precursor. We studied their unique optical properties by using the spectral microreflectometer and their magnetic properties using the superconducting quantum interference device and magnetic force microscopy. Additionally, the resist has the ability to demonstrate both positive and negative resist behaviors depending on the electron beam dosage. With these special characteristics, we can fabricate periodic structure on a thin film possessing controlled optical reflectance properties with one fixed design electron beam pattern without changing the structural parameters but changing the electron beam dosage only. Our approach provides an uncomplicated route for the fabrication of nanometer scale magnetic patterns, which serve as the building blocks in the search for novel properties of periodic magnetic arrays.

I. INTRODUCTION

To understand and compare materials' properties at different scales and further develop useful miniaturized devices, the ability to manage materials at nanoscale is indispensable.[1–4] Conventional fabrication of thin film nanostructures primarily uses selective etching or template growth on the prepatterned resist and then lift-off. However, this approach lacks in the ability to control the position of the nanostructure. Using an electron beam to create nanopatterned materials, such as ZnO, ZrO_2, PZT,[5–7] and so on, is a much easier way to achieve the goal. Yet, all of these have negative nanoscale patterns. A zwitterresist[8,9] refers to a resist that can exhibit both positive and negative properties depending on the applied electron beam dosage. Since the resist possesses both positive and negative patterning capabilities, this will benefit direct electron beam writing technologies. In resist developing processes, the solvents used are often volatile and toxic and thus cause health hazards and environmental pollution. Moreover, these solvents significantly increase the cost of lithography processing. To address this, many new environmentally friendly lithographic processes have been designed for developing resists using either water-developable solutions or supercritical carbon dioxide.[10–13]

Electron-beam lithography has been widely used to fabricate 2D photonic crystals at nanoscale.[14–16] Photonic crystals are macroscopic dielectric media arranged in periodic structures. Yablonovitch[17] and John[18] first described photonic crystals in 1987. Photonic crystals exhibit photonic band gaps that are similar to the electronic band gap of material. Therefore, one can control the propagation of light by restricting its allowable direction at certain frequencies or by localizing light in specific areas. This technology is expected to have a tremendous impact on optical communication applications. The formation of a photonic band gap created by periodically varying the refractive indices can be used to guide the propagation of light as well as to enhance spontaneous emission. It thus has great potential in the development of optoelectronic devices and gives rise to the possibility of optically integrated circuits.[19–21] High refractive index metal oxides patterned by electron beams will be useful for this application. Additionally, if the metal oxide exhibits magnetic properties, its patterned structure will yield interesting and useful optical and magnetic properties.

Recently, perovskite-based manganese oxides have attracted extensive scientific and technological attention. Partially substituting La^{3+} in functional ceramics such as $LaMnO_3$ with divalent ions like Ca^{2+} or Sr^{2+} generates a number of spectacular properties. Most significant is the production of colossal magnetoresistance

[a)]Address all correspondence to this author.
e-mail: suwf@ntu.edu.tw
DOI: 10.1557/JMR.2009.0049

(CMR) in these manganese oxide materials. Manganite thin films possessing CMR have many potential applications including field sensors and recording devices. For crystal structure study,[22–24] several reports describe the lattice parameters a_o, b_o, and c_o of the orthorhombic $La_{1-x}Ca_xMnO_3$ perovskites decrease when the composition x increases. The magnetic properties of $La_{1-x}Ca_xMnO_3$ and its physical properties have been thoroughly investigated.[25–29] Undoped $LaMnO_3$ is an insulating super exchange antiferromagnet. Divalent substitution of La^{3+} leads to a mixed valences of Mn^{3+} and Mn^{4+}. The $La_{1-x}Ca_xMnO_3$ compounds with the composition ratio x to be $0.15 \leq x \leq 0.5$ exhibit a ferromagnetic (FM) ground state and CMR effects are closely associated with a metal-insulator (MI) transition at $T_{MI} \approx T_C$. Recently, the existence of a canted antiferromagnetic state for $La_{1-x}Ca_xMnO_3$ compounds with $x < 0.2$ has been reported from low-field DC magnetization measurements.[30] Theoretically, it is predicted that by increasing the concentration of Mn^{4+}, the antiferromagnetic state would first go through a canted antiferromagnetic state before transforming to an FM state.[31] Therefore, the observation of a canted state for low-x-value $La_{1-x}Ca_xMnO_3$ compounds is significant. However, the magnetic nature of the compositions with $0.4 \leq x \leq 0.5$, which are in the ferro-antiferromagnetic boundary, is not clear.

In our previous report,[32,33] we developed a simple and convenient method for the fabrication of nanoscale patterns of $La_{0.7}Sr_{0.3}MnO_3$ resist films with some unique features and the same method is extended for the development of $La_{0.6}Ca_{0.4}MnO_3$ resist films. Our $La_{0.6}Ca_{0.4}MnO_3$ resist shows some advantages compared with our previous $La_{0.7}Sr_{0.3}MnO_3$ resist. The $La_{0.7}Sr_{0.3}MnO_3$ resist needs to form a pure crystalline phase at 900 °C but the pure crystalline phase temperature for the $La_{0.6}Ca_{0.4}MnO_3$ resist can be lowered to 700 °C for 4 h. Since the nanoscale magnetic array is fabricated first by electron-beam lithography, using a lower sintering temperature can prevent pattern distortion. Furthermore, $La_{0.6}Ca_{0.4}MnO_3$ exhibits stronger magnetization than the previously studied $La_{0.7}Sr_{0.3}MnO_3$. Here, we report a direct writing resist of $La_{0.6}Ca_{0.4}MnO_3$ synthesized from its precursor solution, and the solution functions as a resist via an auto ignition mechanism during electron beam irradiation. Additionally, the resist has the ability to demonstrate both positive and negative resist behaviors depending on the electron beam dosage. With these special characteristics, we can fabricate a periodic structure on a thin film possessing controlled optical reflectance properties with one fixed design electron beam pattern without changing the structural parameters but by simply changing the electron beam dosage. At the same time, our approach provides an uncomplicated route for the fabrication of nanoscale magnetic patterns, which serve as the building blocks in the search for novel properties of periodic magnetic arrays.

II. EXPERIMENTAL SECTION

In this experiment, the electron beam resist was prepared by dissolving 12.33 wt% of lanthanum nitrate [$La(NO_3)_3 \cdot 6H_2O$, Acros, 98%], calcium nitrates [$Ca(NO_3)_2 \cdot 4H_2O$, Acros, 98%], manganese nitrates [$Mn(NO_3)_2 \cdot 4H_2O$, Fluka, 97%] and 1.96 wt% polyvinyl alcohol (Acros, 88%, 22,000 g/mol) in water with a molar ratio of La:Ca:Mn=0.6:0.4:1. The solution was stirred for 48 h at 50 °C. Then the $La_{0.6}Ca_{0.4}MnO_3$ resist was spin coated at 3000 rpm for 90 s to give a nominal thickness of about 300 nm. The thickness of water-developable $La_{0.6}Ca_{0.4}MnO_3$ resist coated on the substrate (indium tin oxide conductive glass or silicon wafer) was measured directly by an alpha-stepper (Veeco, Tektak3). High-resolution nanolithography was performed by using a Elionix ELS-7500EX machine operating at 100 kV with a probe current of 1.0 nA to write the specific patterns across the 150 × 150 μm field with a 2.5 nm beam step size. A sample containing a 3 × 3 array field was exposed with a start dose time of 1 μs, then with an additional dose increment of 0.01, 0.1, and 1 μs per field. The exposed samples were then developed using pure water for 30 s.

The $La_{0.6}Ca_{0.4}MnO_3$ powder samples sintered at different temperatures were analyzed by scanning electron microscopy (SEM) equipped with energy dispersive x-ray spectrometry (EDS, Philips, XL-30, The Netherlands) for chemical composition analysis, and an x-ray diffractometer (XRD, PW 1830, Philips, The Netherlands) for the crystalline structure analysis. The patterned $La_{0.6}Ca_{0.4}MnO_3$ samples were measured by atomic force microscopy (AFM, Digital Instruments, Dimension-3100 Multimode) for surface morphology and surface roughness, and the microstructures of patterned $La_{0.6}Ca_{0.4}MnO_3$ samples were observed by field-emission scanning electron microscope (FE-SEM, Elionix, ERA-8800FE, Japan).

For optical measurement, the refractive indexes of $La_{0.6}Ca_{0.4}MnO_3$ thin films sintered at different temperatures were evaluated by a prism coupler (Metricon Corporation, Metricon-2010). The optical properties of absorbance and reflectance of the patterned $La_{0.6}Ca_{0.4}MnO_3$ samples were studied using a spectral microreflectometer (Mission Peaks Optics, MP100-ME) equipped with an optical microscope. Unpolarized light was focused on the film at a spot size <30 μm. This instrument measured the interference between the incident and reflected light with wavelengths ranging from ultraviolet to near infrared (250–1000 nm).

For magnetic measurement, the magnetic properties of $La_{0.6}Ca_{0.4}MnO_3$ and $La_{0.7}Sr_{0.3}MnO_3$ powders sintered at different sintering conditions were measured by superconducting quantum interference device (SQUID, Quantum Design, MPMS-XL7). For nanoscale magnetic properties in patterned $La_{0.6}Ca_{0.4}MnO_3$ samples, the magnetic phase shift and surface morphology of the samples were measured by Magnetic Force Microscopy (MFM, Digital Instruments, Dimension-3100 Multimode) using the phase detection method.

III. DISCUSSION AND RESULTS

A. Dual functions of the water developable $La_{0.6}Ca_{0.4}MnO_3$ electron beam resist

The $La_{0.6}Ca_{0.4}MnO_3$ resist exhibits dual functions. It can change from negative resist to positive resist with an increase in electron beam dosage and then back to negative resist with further increase in electron beam dosage. Figure 1 illustrates the atomic force microscopy (AFM, Digital Instruments, Dimension-3100 Multimode) images of $La_{0.6}Ca_{0.4}MnO_3$ patterns on the silicon wafer substrate with different electron beam dosages. Films made from the $La_{0.6}Ca_{0.4}MnO_3$ electron beam resist are smooth with an RMS of 1.02 nm, and a thickness of ~200 nm. Figure 1(a) shows the AFM image of a regular triangular array of 150 nm diameter and 500 nm lattice constant of the $La_{0.6}Ca_{0.4}MnO_3$ pillars made with an electron beam dosage of 3.2 mC/cm^2. This step indicates that the $La_{0.6}Ca_{0.4}MnO_3$ resist can be fabricated into negative patterns due to the crosslinking of PVA.[33–35] With an increase in electron beam dosage, the thermal energy from the electron beam transfers to the neighboring area, causing all the PVA to crosslink. Figure 1(b) illustrates the AFM image of the resist in a regular triangular array with an electron beam dosage of 16.0 mC/cm^2. As illustrated in Fig. 1(b), the electron beam resist starts an auto ignition process for the $La_{0.6}Ca_{0.4}MnO_3$ resist at the direct beam location, and results in the formation of loose $La_{0.6}Ca_{0.4}MnO_3$ particles that can be removed using water. Finally, the $La_{0.6}Ca_{0.4}MnO_3$ resist becomes a negative pattern with further increase in electron beam dosage to 450.0 mC/cm^2 [Fig. 1(c)]. Above this electron beam threshold, the thermal energy can promote densification and obtain a pure $La_{0.6}Ca_{0.4}MnO_3$ phase. In this stage, the thermal energy of the electron beam transfers to the neighboring area and creates loose $La_{0.6}Ca_{0.4}MnO_3$ particles in the area via auto ignition. These loose particles can be easily removed by water and generate the negative pattern. Figure 1(d) illustrates the sensitivity curves of the $La_{0.6}Ca_{0.4}MnO_3$ resist after electron beam irradiation and development. In Fig. 1(d), the A region represents a negative characteristic when the resist is irradiated at a dose of 1.5–4.0 mC/cm^2, the B region exhibits a positive characteristic using a dose of 15.0–30.0 mC/cm^2, and the C region shows a negative characteristic using a dose of 300.0–500.0 mC/cm^2. Although the dose of the exposure of this $La_{0.6}Ca_{0.4}MnO_3$ resist is very high in comparison to most organic resists, the $La_{0.6}Ca_{0.4}MnO_3$ resist generates active electromagnetic functional nanopatterns in one step whereas the use of organic resists generating $La_{0.6}Ca_{0.4}MnO_3$ nanopatterns involves three steps: (i) fabricate nanopatterns from organic resist, (ii) deposit $La_{0.6}Ca_{0.4}MnO_3$ on the nanopatterns, and (iii) remove organic resist. The use of $La_{0.6}Ca_{0.4}MnO_3$ will not only reduce process steps but also use no environmentally harmful organic chemicals as compared to the organic resist.

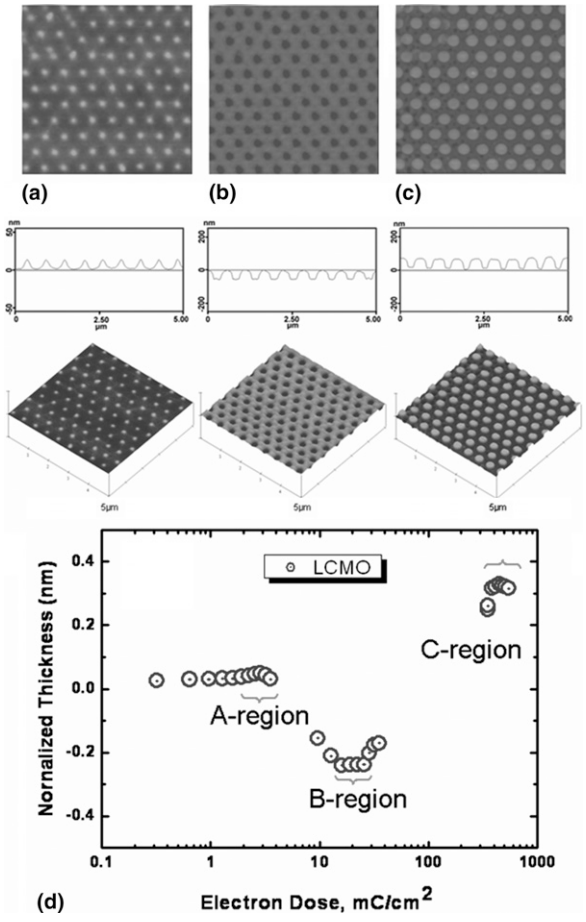

FIG. 1. Two-dimensional, cross-sectional, and three-dimensional atomic force microscopy images of $La_{0.6}Ca_{0.4}MnO_3$ resist irradiated by different electron beam dosages. (a) Negative pattern (3.2 mC/cm^2), (b) positive pattern (16.0 mC/cm^2), and (c) negative pattern (450.0 mC/cm^2). (d) The sensitivity curves of the water-developable $La_{0.6}Ca_{0.4}MnO_3$ resists after electron beam irradiation and development.

To understand the thermal behavior of the $La_{0.6}Ca_{0.4}MnO_3$ resist due to the thermal energy from the electron beam, we carried out parallel thermal experiments for the $La_{0.6}Ca_{0.4}MnO_3$ resist. First, we removed water from the $La_{0.6}Ca_{0.4}MnO_3$ solution to form a gel, and then subjected the gel to differential

scanning calorimetry (DSC, DuPont, TA 2910) and thermogravimetry (TGA, DuPont, TA 2950) analyses (Fig. 2). The DSC thermogram shows many exothermic peaks, one of them is ranged from 100 to 150 °C which is due to the crosslinking of PVA. The TGA curve illustrates a major decomposition at around 208 °C. This is indicative of the auto ignition behavior as shown by a sharp and nearly vertical step. The result is consistent with an intense exothermic peak at 234 °C in the DSC. This type of decomposition with a sharp and intense exotherm implies a self-propagation combustion process that has been observed in other systems. The auto ignition of the gel occurs by a thermally induced oxidation-reduction reaction where the PVA acts as a fuel and NO_3^- acts as an oxidant. The auto ignition can be induced by mixing an appropriate ratio of the fuel and the oxidant, giving rise to a single-step decomposition associated with a particular reaction temperature and appreciable exothermicity, so as to facilitate the formation of $La_{0.6}Ca_{0.4}MnO_3$.

Figure 3 reveals the x-ray diffraction patterns of the $La_{0.6}Ca_{0.4}MnO_3$ electron beam resist powder samples sintered at different temperatures. The sample sintered at 250 °C clearly indicates formation of the high symmetry orthorhombic phase of $La_{0.6}Ca_{0.4}MnO_3$ containing a little amount of La_2O_3 impurity (~29°). The sample sintered at 700 °C indicates the structure is a pure orthorhombic phase of $La_{0.6}Ca_{0.4}MnO_3$. All the peaks can be perfectly indexed as the pure orthorhombic phase [Pnma (62), JCPDS No. 46-0513] of $La_{0.6}Ca_{0.4}MnO_3$, with lattice constants a = 5.443 Å, b = 7.683 Å, and c = 5.454 Å. Therefore, the patterned $La_{0.6}Ca_{0.4}MnO_3$ made by electron-beam lithography plus post sintering at 700 °C for 4 h can form a pure orthorhombic phase. A high saturation magnetization has been measured for this sample and we will discuss these details in the magnetic properties section.

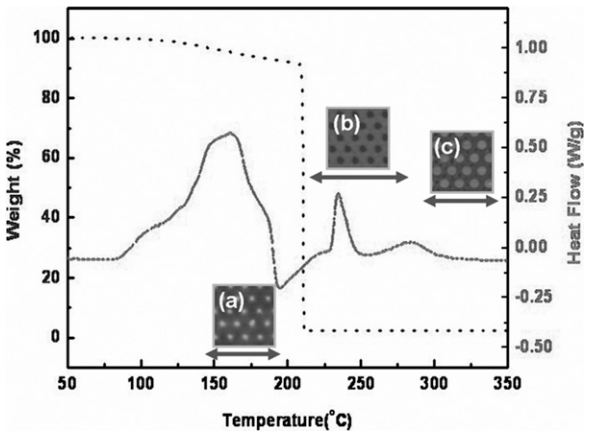

FIG. 2. Differential scanning calorimetry analysis (solid line) and thermal gravimetric analysis (dotted line) of a $La_{0.6}Ca_{0.4}MnO_3$ electron beam resist. (a)–(c) are the patterns obtained at different electron beam dosages corresponding to the different temperature range.

An energy-dispersive x-ray analysis (SEM-EDAX, Philips, XL-30, The Netherlands) was used to monitor the amount of elemental C and N in the $La_{0.6}Ca_{0.4}MnO_3$ resist prepared either by thermal treatment or by electron beam irradiation (Table I). The elemental C and N come from the PVA and metallic nitrates, respectively, and thus they can be used to indicate the formation of the orthorhombic phase. The electron beam irradiated samples (450 mC/cm^2) contain fewer amounts of both elements than the heat treated samples at 300 °C for 4 h. From the XRD data, we know the orthorhombic $La_{0.6}Ca_{0.4}MnO_3$ can be formed at 300 °C or above. Therefore, the results reveal that the orthorhombic $La_{0.6}Ca_{0.4}MnO_3$ was formed by the electron beam irradiation of the resist.

Figure 4 shows the scanning electron microscopic (SEM) photographs of a patterned $La_{0.6}Ca_{0.4}MnO_3$ resist made by electron-beam lithography. Figure 4(a) shows a line pattern with a width of 80 nm and an interval (distance between lines) of 300 nm. Figure 4(b) shows an array pattern with a width of 200 nm and an interval of 1000 nm. Figures 4(c) and 4(d) clearly show that both positive and negative patterns can be obtained from $La_{0.6}Ca_{0.4}MnO_3$ resist. Figure 4(c) is a triangular periodic air hole array with a lattice constant of 500 nm, an air hole diameter of 250 nm, and an average depth of 60 nm.

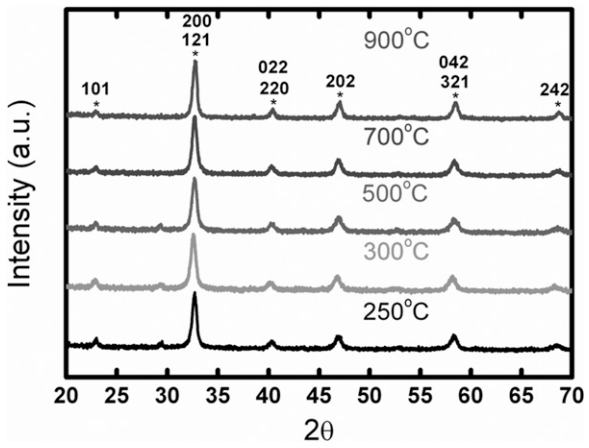

FIG. 3. X-ray diffraction patterns of water-developable $La_{0.6}Ca_{0.4}MnO_3$ electron beam resist sintered at different temperatures for 4 h.

TABLE I. Energy-dispersive x-ray analysis of carbon and nitrogen elements in the water-developable $La_{0.6}Ca_{0.4}MnO_3$ electron beam resist at different fabricated conditions.

Condition	Carbon (wt%)	Nitrogen (wt%)
Electron beam (450 mC/cm^2)	3.01	0.57
250 °C, 4 h	4.69	0.63
300 °C, 4 h	3.54	0.61
500 °C, 4 h	2.39	0.55
700 °C, 4 h	1.81	0.33

In contrast, Fig. 4(d) shows a pillar array of $La_{0.6}Ca_{0.4}MnO_3$ with a 250 nm diameter, 500 nm lattice constant, and an average height of 60 nm.

B. Tunable optical properties of patterned $La_{0.6}Ca_{0.4}MnO_3$

In conventional electron-beam lithography, one can easily adjust the reflectivity of a 2D photonic crystal by simultaneously varying the *x*, *y* axial shape and periodicity, while maintaining the *z* axial height. Our dual function and high refractive index $La_{0.6}Ca_{0.4}MnO_3$ electron beam resist can regulate the *z* axial height as well by varying the electron irradiation at fixed *x*, *y* axial geometry and periodicity. As discussed above, the formation of $La_{0.6}Ca_{0.4}MnO_3$ patterns are due to the heat generated from the electron beam irradiation. In this study, quantifying the refractive index is the key to understanding the optical properties of the electron beam patterned $La_{0.6}Ca_{0.4}MnO_3$. However, the refractive index of the electron beam patterned $La_{0.6}Ca_{0.4}MnO_3$ sample is too small to be measured accurately using the conventional ellipsometer or prism coupler method. Therefore, we measured the refractive index of the thermal sintered $La_{0.6}Ca_{0.4}MnO_3$ samples with the applied thermal energies equivalent to that of the electron beam. Table II summarizes the refractive indices of the $La_{0.6}Ca_{0.4}MnO_3$ thin film samples prepared at different sintering conditions. The negative pattern obtained at a low electron beam dose has a refractive index of 2.02 whereas the negative pattern obtained at a high electron beam dose has a higher refractive index of 2.34. For the medium electron dose sample, it has a rather low refractive index of 2.02 because of the fabrication process. As the exposed area is removed, the remaining area becomes a mixture of PVA and $La_{0.6}Ca_{0.4}MnO_3$ precursor salts, whose composition is the same as the low electron dose sample and thus has the same refractive index value. Therefore, we can change the refractive index of the resist by varying the electron beam dosage.

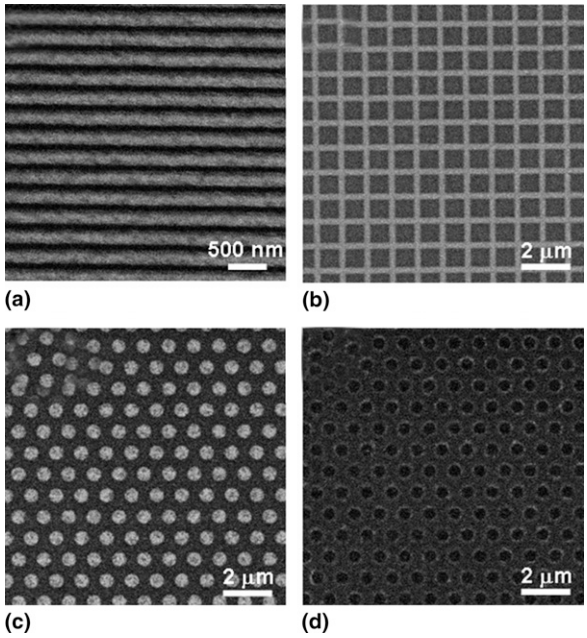

FIG. 4. Scanning-electron-microscopy (SEM) images of patterned $La_{0.6}Ca_{0.4}MnO_3$ electron beam resist. (a) Periodic lines with a width of 80 nm and an interval of 300 nm, (b) an array pattern with a width of 200 nm and an interval of 1000 nm, (c) a positive pattern with triangular $La_{0.6}Ca_{0.4}MnO_3$ periodic holes with a lattice constant of 500 nm (the diameter of the light-colored circle is 250 nm), and (d) a negative pattern of pillars in a regular array with a 250 nm diameter and a 500 nm lattice constant.

The different reflectance spectra of the patterned $La_{0.6}Ca_{0.4}MnO_3$ samples are shown in Fig. 5. Each curve shown in the figure represents a sample obtained at a specific electron irradiation as indicated at the right side of the curves. The reflectance of each curve was measured by a spectral microreflectometer equipped with an optical microscope. This instrument measures the interference between the incident and the reflected light with wavelengths ranging from ultraviolet to the near infrared range (250–1000 nm). Unpolarized light was focused on the sample to a spot size of <30 μm. The thickness of the $La_{0.6}Ca_{0.4}MnO_3$ electron beam resist coated on the indium tin oxide conductive glass substrate is about 300 nm. A 50 × 50 μm sample with a regular triangular array pattern of 500 nm diameter and 1000 nm lattice constant was prepared. By increasing the electron beam dosage, we obtained dramatically different geometries of patterned $La_{0.6}Ca_{0.4}MnO_3$ that produced changes in the reflectance spectra. The negative patterned $La_{0.6}Ca_{0.4}MnO_3$ exhibits two peaks with λ_{max} at 445 and 480 nm [Fig. 5, curves (a) and (b)] in the A region was obtained by electron irradiation at 1.5–4.0 mC/cm^2. The positive patterned $La_{0.6}Ca_{0.4}MnO_3$ in the B region was obtained at an electron beam dosage of 15.0–30.0 mC/cm^2. The reflectance peaks of region B samples have been red-shifted from 445 and 480 nm

TABLE II. Summary of refractive indices of $La_{0.6}Ca_{0.4}MnO_3$ samples prepared at different sintering conditions.

Sample No.	Sintering condition	Refractive index	Pattern characteristic	Equivalent electron beam dosage (mC/cm^2)
1	—	~2.00	—	0.0
2	150 °C, 4 h	~2.02	Negative	1.5–4.0 (A region)
3	250 °C, 4 h	~2.02	Positive	15.0–30.0 (B region)
4	300 °C, 4 h	~2.34	Negative	300.0–500.0 (C region)

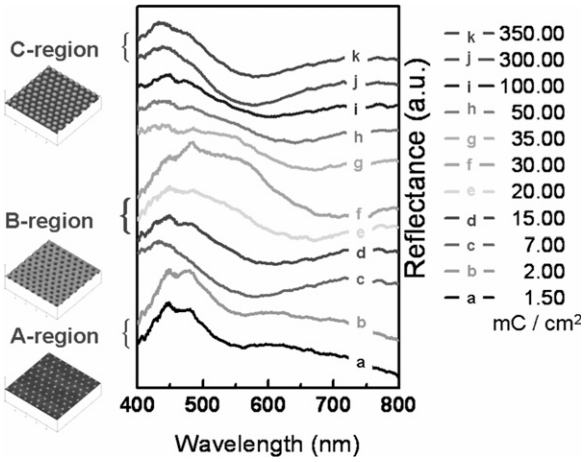

FIG. 5. The reflectance spectra of patterned $La_{0.6}Ca_{0.4}MnO_3$ fabricated at different electron beam dosages. The reflectance peak changes with the electron beam dosage are shown in the center part of the figure.

to 450 and 485 nm, respectively. [Fig. 5, curves (a) and (b) versus (d)–(f)]. This red shift is due to changes in air column geometries of the *z*-axis. The height of the air column in the patterned $La_{0.6}Ca_{0.4}MnO_3$ decreases gradually with increasing electron dosage, which is confirmed by AFM measurements of samples and seen as curves (d) and (f). These interesting results indicate we can use patterned $La_{0.6}Ca_{0.4}MnO_3$ to modulate the light wavelength by applying a different electron beam dosage without changing the designed pattern. This particular feature is expected since the frequency of a light beam ($f = \omega a/2\pi c = a/\lambda$) is inversely related to the dielectric constant, ε, of the media ($f \propto 1/\sqrt{\varepsilon}$). From this, the wavelength increases as the dielectric constant of the media is increased by decreasing the air column height. The observed change in reflectance peaks from curve (f) to curve (g) are due to the geometry changes from a negative to a positive pattern associated with the refractive index decreasing (less material from electron beam etching). From curve (g) to curve (k), the heights and the refractive indices of the $La_{0.6}Ca_{0.4}MnO_3$ pillars increase gradually but the amount of material decreases with a decrease in the dielectric constant; the $La_{0.6}Ca_{0.4}MnO_3$ sample exhibits a clear blue shift reflectance maximum at 425 nm as marked by region C of Fig. 5.

C. Magnetic properties of $La_{0.6}Ca_{0.4}MnO_3$ resist and patterned $La_{0.6}Ca_{0.4}MnO_3$

The magnetic properties of the $La_{0.6}Ca_{0.4}MnO_3$ electron beam resist were first studied as powdered samples, because it was difficult to fabricate a sample with a large enough area for magnetic measurements. We compared the magnetic properties of $La_{0.6}Ca_{0.4}MnO_3$ with $La_{0.7}Sr_{0.3}MnO_3$ synthesized using similar methods.[33,34] $La_{0.6}Ca_{0.4}MnO_3$ powder was prepared by drying the

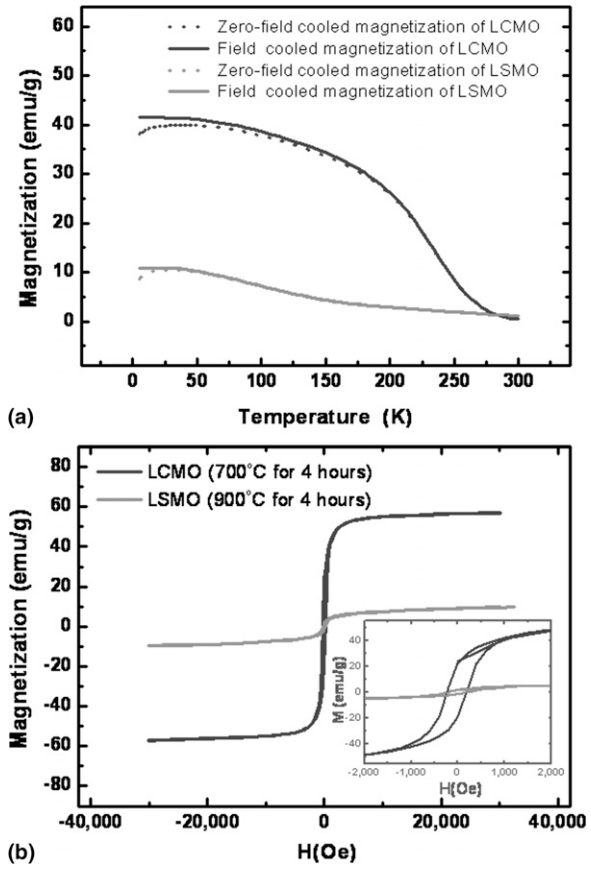

FIG. 6. (a) The zero-field cooled magnetization and field cooled magnetization for $La_{0.6}Ca_{0.4}MnO_3$ and $La_{0.7}Sr_{0.3}MnO_3$, respectively at an applied field of 1000 Oe. (b) The hysteresis loops of $La_{0.6}Ca_{0.4}MnO_3$ and $La_{0.7}Sr_{0.3}MnO_3$ powders at 10 K; the inset shows the hysteresis loops at enlarged scale.

resist material at 120 °C for 12 h and sintering at 700 °C for 4 h. The $La_{0.7}Sr_{0.3}MnO_3$ powder was prepared by drying the resist material at 120 °C for 12 h and sintering at a higher temperature of 900 °C for 4 h. The results are shown in Fig. 6. In our previous study, the $La_{0.7}Sr_{0.3}MnO_3$ resist needs to form a pure crystalline phase at 900 °C but the pure crystalline phase temperature for the $La_{0.6}Ca_{0.4}MnO_3$ resist can be lowered to 700 °C for 4 h. Because these magnetic arrays are fabricated first by electron-beam lithography, applying a lower sintering temperature can prevent pattern distortion. Both samples were magnetized in one direction, and they did not relax back to zero magnetization when the imposed magnetizing field was removed. Furthermore, the magnetizing field imposed on $La_{0.6}Ca_{0.4}MnO_3$ causes a larger magnetization than that on $La_{0.7}Sr_{0.3}MnO_3$. These results indicate that $La_{0.6}Ca_{0.4}MnO_3$ more readily forms the pervoskite structure and is more easily magnetized than $La_{0.7}Sr_{0.3}MnO_3$.

The $La_{0.6}Ca_{0.4}MnO_3$ powders sintered at different temperatures were measured by SQUID at 10 K as

shown in Fig. 7. The magnetization of $La_{0.6}Ca_{0.4}MnO_3$ powders sintered at 250, 300, and 500 °C have almost the same saturation magnetization of ±40 emu/g under 30,000 Oe at 10 K. However, the $La_{0.6}Ca_{0.4}MnO_3$ powder sample sintered at 700 °C exhibits a saturation magnetization of ±60 emu/g under 30,000 Oe at 10 K. This shows the saturation magnetization of $La_{0.6}Ca_{0.4}MnO_3$ changes with different sintering temperatures. Moreover, the differences of saturation magnetization of $La_{0.6}Ca_{0.4}MnO_3$ are due to the formation of the pure $La_{0.6}Ca_{0.4}MnO_3$ crystalline phase. The $La_{0.6}Ca_{0.4}MnO_3$ powder sample sintered at 700 °C exhibits the highest saturation magnetization of all the powder samples, because the sample forms a pure $La_{0.6}Ca_{0.4}MnO_3$ crystalline phase after treating at 700 °C for 4 h. The $La_{0.6}Ca_{0.4}MnO_3$ crystalline phases changed by a different sintering temperature are shown in Fig. 3.

The nanoscale magnetic property of patterned $La_{0.6}Ca_{0.4}MnO_3$ was studied by magnetic force microscopy (MFM). MFM uses a scanning probe microscope (SPM) that can map the spatial distribution of magnetism by measuring the magnetic interaction between a sample and the tip. Figures 8(a)–8(f) show the AFM topographic images and the magnetic force gradient images (phase signal) of the samples. The sizes of these images are 5 × 5 μm, and the corresponding scale bars are fixed that 200 nm in topographic images and 10° in phase images, respectively. In MFM mode, the cantilever is lifted up 25 nm higher than in the topography mode. Figures 8(a) and 8(b) illustrate the topographic image and magnetic force gradient image of a sample with a regular triangular pillars array possessing a 330 nm diameter, 500 nm lattice constant, and 65 nm thickness. Although this sample was made by irradiating the $La_{0.6}Ca_{0.4}MnO_3$ resist at an electron dosage of 450.0 mC/cm^2, no magnetic gradient image was observed [Fig. 8(b)]. This result indicates that the $La_{0.6}Ca_{0.4}MnO_3$ sample made by electron-beam lithography without sintering does not obtain the pure $La_{0.6}Ca_{0.4}MnO_3$ orthorhombic structure required for magnetic behavior. Figures 8(c) and 8(d) show the topographic and magnetic force gradient images, respectively, of a regular triangular pillar array with a 250 nm diameter, 500 nm lattice constant, and 60 nm thickness produced by irradiating the $La_{0.6}Ca_{0.4}MnO_3$ resist at an electron dosage of 450.0 mC/cm^2 plus post sintering

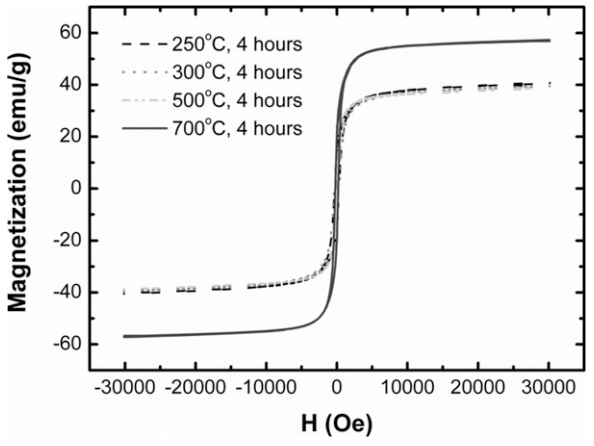

FIG. 7. The hysteresis loops of $La_{0.6}Ca_{0.4}MnO_3$ powder samples sintered at different temperatures for 4 h that were measured by SQUID at 10 K.

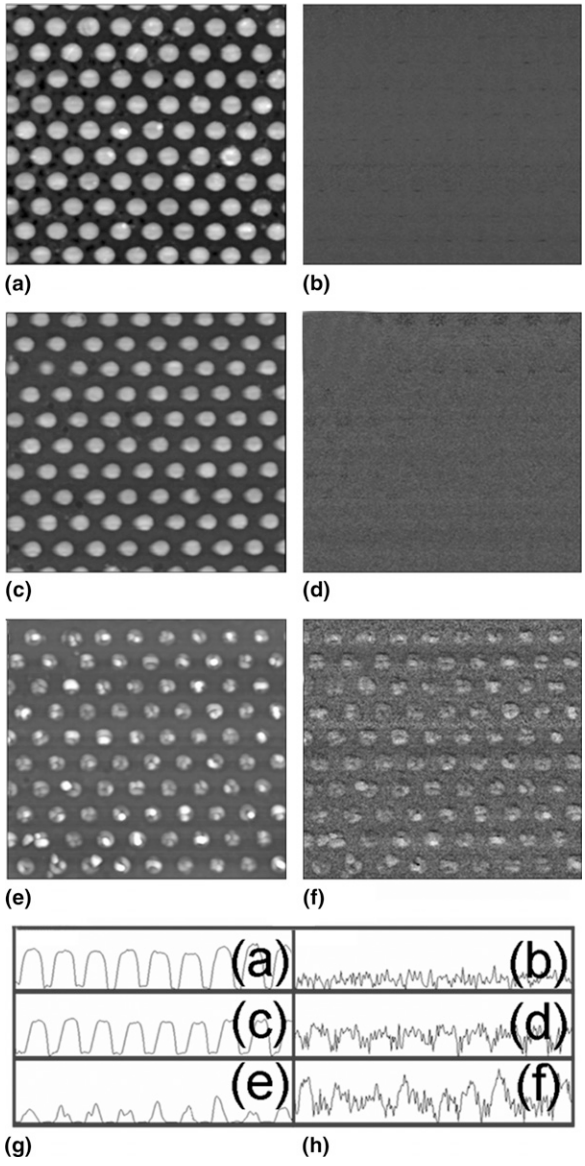

FIG. 8. AFM topographic images and the magnetic force gradient images (phase signal) of the patterned $La_{0.6}Ca_{0.4}MnO_3$. The sizes of these images are 5 × 5 μm, and their data scales are 200 nm and 10°, respectively. (a, b) The patterned $La_{0.6}Ca_{0.4}MnO_3$ sample fabricated at an electron dosage of 450.0 mC/cm^2. (c, d) The patterned sample fabricated at an electron dosage of 450.0 mC/cm^2 plus sintering at 250 °C, 4 h. (e, f) The patterned sample fabricated at an electron dosage of 450.0 mC/cm^2 plus sintering at 700 °C, 4 h. (g) The cross-sectional images of the sample topography. (h) MFM phase shift of three patterned samples.

at 250 °C for 4 h. We did not detect any magnetic behavior for this sample, again indicating that pure $La_{0.6}Ca_{0.4}MnO_3$ orthorhombic structure was not obtained at mild post sintering conditions. These results are consistent with our XRD study. Figures 8(e) and 8(f) show the topographic and magnetic force gradient images, respectively, of a regular triangular pillar array with a 250 nm diameter, 500 nm lattice constant, and 30–35 nm thickness produced by irradiating the resist at an electron dosage of 450.0 mC/cm^2 plus post sintering at 700 °C for 4 h. In Fig. 8(f), the magnetic force gradient can be observed clearly. The $La_{0.6}Ca_{0.4}MnO_3$ resist is completely converted to a pure orthorhombic structure under this fabrication condition. The result is also consistent with our XRD study. To make sure the tip-sample separation distance is large enough to eliminate the van der Waals force, we plotted the cross-sectional images of topography and MFM phase shift of $La_{0.6}Ca_{0.4}MnO_3$ pillars fabricated under different thermal conditions in Figs. 8(g) and 8(h). The size of $La_{0.6}Ca_{0.4}MnO_3$ pillars decreases with increasing sintering temperature as shown in Fig. 8(g). Nevertheless, the MFM phase shift of $La_{0.6}Ca_{0.4}MnO_3$ pillars increases with increasing the sintering temperature in Fig. 8(g). This finding indicates that the MFM results are due to the magnetic force distribution in the sample rather than from the atomic force.

To further confirm the MFM images are indeed due to the magnetic force distribution instead of van der Waals forces, we performed various MFM measurements by changing the tip-sample separation distance (lift scan height). The principle of MFM measurement is based on noncontact atomic force microscopy.[36] Therefore, both atomic force and the magnetic interactions are detected (see Fig. 9). From the aspect of atomic force, neutral atoms and molecules are subjected to two distinct forces correlating to large and short distances. The attractive force is at long range and the repulsive force is at short range. The Lennard-Jones potential[37] is a simple mathematical model that represents this behavior as Eq. (1).

$$V(r) = 4\varepsilon\left[\left(\frac{\sigma}{r}\right)^{12} - \left(\frac{\sigma}{r}\right)^{6}\right] \quad . \qquad (1)$$

where ε is the depth of the potential well, r is the distance between two neutral atoms or two molecules, and σ is the finite distance at which the potential is zero. These parameters can be fitted to reproduce experimental data or deduced from the results of accurate quantum chemistry calculations. The term $(1/r^{12})$ describes repulsion and the term $(1/r^6)$ describes attraction. The force function is the negative of the gradient of the above potential as shown in Eq. (2), and $\hat{r}$ is the vector pointing from one neutral atom or one molecule to the other.

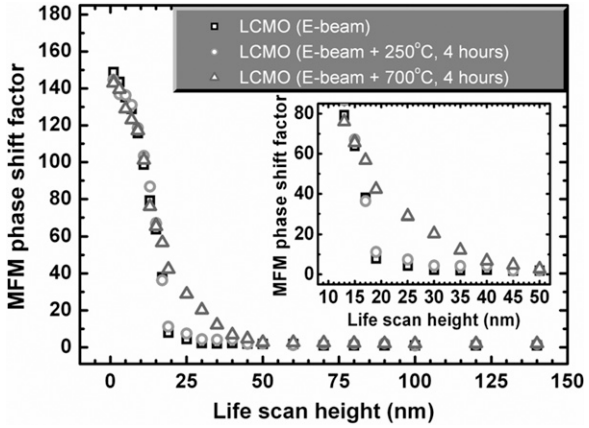

FIG. 9. The MFM phase shift factor, which is proportional to the force acting on the tip, at different tip-sample distances in the MFM and AFM measurements for three patterned $La_{0.6}Ca_{0.4}MnO_3$ samples. (□) The sample fabricated at an electron beam dosage of 450.0 mC/cm^2. (○) The patterned $La_{0.6}Ca_{0.4}MnO_3$ sample fabricated at an electron beam dosage of 450.0 mC/cm^2 plus sintering at of 250 °C, 4 h. (Δ) The sample fabricated at an electron beam dosage of 450.0 mC/cm^2 plus sintering at 700 °C, 4 h.

$$F(r) = -\frac{d}{dr}V(r)\,\hat{r} = 4\varepsilon\left[12\frac{\sigma^{12}}{r^{13}} - 6\frac{\sigma^{6}}{r^{7}}\right]\hat{r} \quad , \qquad (2)$$

The magnetic force equation between two poles abides by Coulomb's law follows the equation given by

$$F = \frac{p_1 p_2}{4\pi\mu_0 r^2} \quad , \qquad (3)$$

where r is the distance between the two poles, p_1 and p_2, and μ_0 is the permeability of empty space that is equal to $4\pi \times 10^{-7}$ weber/ampere meter. Thus, we can see that the van der Waals force decreases with increasing distance more rapidly than the magnetic force. Figure 8 shows the phase shift factor, which is proportional to the force acting on the tip, at different tip-sample distances in the MFM and AFM measurements for three samples (see Fig. 9). The three samples are $La_{0.6}Ca_{0.4}MnO_3$ pillars fabricated by electron-beam lithography (squares), $La_{0.6}Ca_{0.4}MnO_3$ pillars fabricated by electron-beam lithography plus 250 °C sintering for 4 h (circles), and $La_{0.6}Ca_{0.4}MnO_3$ pillars fabricated by electron-beam lithography plus 700 °C sintering for 4 h (triangles). These three $La_{0.6}Ca_{0.4}MnO_3$ pillars have a thickness of about 65, 60, and 35 nm, respectively, and were deposited on silicon wafers. The sample with post sintering treatment at 700 °C for 4 h exhibits a slow magnetic force decrease with increasing tip-sample distance, indicating the sample has a large magnetic moment. On the other hand, the sample without post sintering treatment has a negligible magnetic moment and exhibits a rapid force decrease with increasing tip-sample distance. At small tip-sample distances (<15 nm), the total force is dominated by the atomic force, and the difference between the MFM and AFM

phase images is indistinguishable. When the distance is greater than 15 nm, the magnetic force becomes dominant. Both forces diminish after the distance exceeds 40 nm. The experimental curves are described well by Eqs. (2) and (3). We therefore conclude that a well-defined magnetic pattern has been successfully fabricated using water-developable $La_{0.6}Ca_{0.4}MnO_3$ electron beam resist.

IV. CONCLUSION

In summary, we are able to create magnetic patterns using the environmentally friendly water-developable $La_{0.6}Ca_{0.4}MnO_3$ electron beam resist in one step. Both positive and negative patterns are readily fabricated by varying the electron dosage. The $La_{0.6}Ca_{0.4}MnO_3$ electron beam resist exhibits high refractive index and dual functions, so it can be varied by processing condition and is useful for photonic crystal fabrication. The reflectance spectra of the $La_{0.6}Ca_{0.4}MnO_3$ electron beam resist can be changed in a fixed design pattern because the morphology and the refractive index of the patterned $La_{0.6}Ca_{0.4}MnO_3$ are changed by varying the electron dosage. The magnetic properties of the patterned $La_{0.6}Ca_{0.4}MnO_3$ can be clearly observed by post sintering the sample at 700 °C for 4 h after electron beam writing in our MFM study. We emphasize here that our study provides an environmentally friendly yet simple and convenient approach for the fabrication of magnetic patterns, which underpin many novel properties awaiting future exploration.

ACKNOWLEDGMENTS

Financial support from the National Science Council of Taiwan (NSC-96-2628-E-002-017-MY3 and NSC 95-3114-P-002-003-MY3) is highly appreciated. The authors would also like to thank Prof. C-H. Kuan, Prof. C-F. Lin, Prof. C-W. Chen, Ms. S. Chen, and Mr. Y-Y. Lin of National Taiwan University and Prof. K-C. Cheng of National Taipei University of Technology for helpful discussions, and Mr. A.J. Su of University of Pittsburgh for editing the manuscript. The electron beam lithography was carried out using the Elionix's facility located at the National Taiwan University Center for Information and Electronics Technologies.

REFERENCES

1. C.S. Wu, C.F. Lin, H.Y. Lin, C.L. Lee, and C.D. Chen: Polymer-based photonic crystals fabricated with single-step electron-beam lithography. *Adv. Mater.* **19**(19), 3052 (2007).
2. Y.L. Chueh, M.T. Ko, L.J. Chou, L.J. Chen, C.S. Wu, and C.D. Chen: $TaSi_2$ nanowires: A potential field emitter and interconnect. *Nano Lett.* **6**(8), 1637 (2006).
3. S.B. Clendenning, S. Aouba, M.S. Rayat, D. Grozen, J.B. Sorge, P.M. Broderson, R.M.S. Sodhi, Z.H. Lu, C.M. Yip, M.R. Freeman, H.E. Ruda, and I. Manners: Direct writing of patterned ceramics using electron-beam lithography and metallopolymer resists. *Adv. Mater.* **16**(3), 215 (2004).
4. M.J. MacLachlan, M. Ginzburg, N. Coombs, T.W. Coyle, N.P. Raju, J.E. Greedan, G.A. Ozin, and I. Manners: Shaped ceramics with tunable magnetic properties from metal-containing polymers. *Science* **287**, 1460 (2000).
5. M.S.M. Saifullah, K.R.V. Subramanian, D.J. Kang, D. Anderson, W.T.S. Huck, G.A.C. Jones, and M.E. Welland: Sub-10 nm high-aspect-ratio patterning of ZnO using an electron beam. *Adv. Mater.* **17**(14), 1757 (2005).
6. K.R.V. Subramanian, M.S.M. Saifullah, E. Tapley, D.J. Kang, M.E. Welland, and M. Butler: Direct writing of ZrO_2 on a sub-10 nm scale using an electron beam. *Nanotech.* **15**(1), 158 (2004).
7. M. Alexe, C. Harnagea, A. Visinoiu, A. Pignolet, D. Hesse, and U. Gösele: Patterning and switching of nano-size ferroelectric memory cells. *Scr. Mater.* **44**(8), 1175 (2001).
8. J.K. Chen, F.H. Ko, H.L. Chen, and F.C. Chang: Mechanism and modeling of ring pattern formation for electron beam exposure on zwitterresist. *Jpn. J. Appl. Phys.* **42**, 3838 (2003).
9. J.K. Chen, F.H. Ko, and F.C. Chang: Structural transformation of acrylic resin upon controlled electron-beam exposure yields positive and negative resists. *Adv. Funct. Mater.* **15**(7), 1147 (2005).
10. Q. Lin, T. Steinhäusler, L. Simpson, M. Wilder, D.R. Medeiros, C.G. Willson, J. Havard, and J.M.J.A. Fréchet: Water-castable, water-developable chemically amplified negative-tone resist. *Chem. Mater.* **9**(8), 1725 (1997).
11. J.M. Havard, S.Y. Shim, J.M.J. Fréchet, Q. Lin, D.R. Medeiros, C.G. Willson, and J.D. Byers: Design of photoresists with reduced environmental impact. 1. Water-soluble resists based on photo-cross-linking of poly(vinyl alcohol). *Chem. Mater.* **11**(3), 719 (1999).
12. J.M. Havard, N. Vladimirov, J.M.J. Fréchet, S. Yamada, C.G. Willson, and J.D. Byers: Photoresists with reduced environmental impact: Water-soluble resists based on photo-cross-linking of a sugar-containing polymethacrylate. *Macromol.* **32** (1), 86 (1999).
13. I.A. Cooper: Recent developments in materials synthesis and processing using supercritical CO_2. *Adv. Mater.* **13**(14), 1111 (2001).
14. J.Y. Cheng, C.A. Ross, H.I. Smith, and E.L. Thomas: Templated self-assembly of block copolymers: Top-down helps bottom-up. *Adv. Mater.* **18**(19), 2505 (2006).
15. J.R. Cao, P.T. Lee, S.J. Choi, J.D. Dapkus, and P.D. Dapkus: Lithographic fine-tuning of vertical cavity surface emitting laser-pumped two-dimensional photonic crystal lasers. *J. Nanosci. Nanotechnol.* **2**(3–4), 313 (2002).
16. Y.L. Chen, C.C. Chen, J.C. Jeng, and Y.F. Chen: Enhancement of optical properties of CdSe pillars fabricated by the combination of electron-beam lithography and electrochemical deposition. *Appl. Phys. Lett.* **85**(7), 1259 (2004).
17. E. Yablonovitch: Inhibited spontaneous emission in solid-state physics and electronics. *Phys. Rev. Lett.* **58**(20), 2059 (1987).
18. S. John: Strong localization of photons in certain disordered dielectric superlattices. *Phys. Rev. Lett.* **58**(23), 2486 (1987).
19. F. Fleischhaker and R. Zentel: Photonic crystals from core-shell colloids with incorporated highly fluorescent quantum dots. *Chem. Mater.* **17**(6), 1346 (2005).
20. Q. Yan, Z. Zhou, and X.S. Zhao: Introduction of three-dimensional extrinsic defects into colloidal photonic crystals. *Chem. Mater.* **17**(12), 3069 (2005).
21. C.M. Chuang, W.B. Lu, W.F. Su, C.M. Lin, and Y.F. Chen: Manipulation of luminescence from CdSe nanoparticles by 3-D photonic crystal. *J. Appl. Phys.* **97**, 096104 (2005).
22. P. Srivastava, O.N. Srivastava, H.K. Singh, and P.K. Siwach: Synthesis and magnetotransport properties of Mm-doped $La_{0.7}Ca_{0.3}MnO_3$. *J. Alloys Compd.* **459**(1–2), 61 (2008).

23. F.L. Tang and X.V. Zhang: Atomic distribution and local structure in charge-ordered $La_{1/3}Ca_{2/3}MnO_3$. *Phys. Rev. B: Condens. Matter* **73**(14), 144401 (2006).
24. B. Dabrowski, R. Dybzinski, Z. Bukowski, O. Chmaissem, and J.D. Jorgensen: Oxygen content and structures of $La_{1-x}Ca_xMnO_{3+d}$ as a function of synthesis conditions. *J. Solid State Chem.* **146**(2), 448 (1999).
25. S. Mori, C.H. Chen, and S.W. Cheong: Pairing of charge-ordered stripes in (La,Ca)MnO_3. *Nature* **392**(6675), 473 (1998).
26. C.H. Chen, S.W. Cheong, and H.Y. Hwang: Charge-ordered stripes in $La_{1-x}Ca_xMnO_3$ with $x > 0.5$. *J. Appl. Phys.* **81**(8), 4326 (1997).
27. S. Jin, T.H. Tiefel, M. McCormack, R.A. Fastnacht, R. Ramesh, and L.H. Chen: Thousandfold change in resistivity in magnetoresistive La-Ca-Mn-O films. *Science* **264**(5157), 413 (1994).
28. K.H. Kim, S. Lee, T.W. Noh, and S.W. Cheong: Charge ordering fluctuation and optical pseudogap in $La_{1-x}Ca_xMnO_3$. *Phys. Rev. Lett.* **88**(16), 167204 (2002).
29. A. Das, K.R. Chakraborty, S.S. Gupta, S.K. Kulshreshtha and S.K. Paranjpe: Structural and magnetic ordering in $La_{0.6}Ca_{0.4}MnO_3$. *J. Magn. Magn. Mater.* **237**(1), 41 (2001).
30. R. Laiho, K.G. Lisunov, E. Lahderanta, P. Petrenko, V.N. Stamov, and V.S. Zakhvalinskii: Low-field magnetic properties of $La_{1-x}Ca_xMnO_3$ ($0 < x < 0.4$). *J. Magn. Magn. Mater.* **213**(3), 271 (2000).
31. P.G.D. Gennes: Effects of double exchange in magnetic crystals. *Phys. Rev.* **118**(1), 141 (1960).
32. M.C. Wu, C.M. Chuang, Y.F. Chen, and Y.F. Su: Fabrication and optical properties of periodical structures based on a water-developable and tunable $La_{0.7}Sr_{0.3}MnO_3$ resist. *J. Mater. Chem.* **18**, 780 (2008).
33. C.M. Chuang, M.C. Wu, Y.C. Huang, K.C. Cheng, C.F. Lin, Y. F. Chen, and Y.F. Su: Nanolithography made from water-based spin-coatable LSMO resist. *Nanotechnology* **17**(14), 4399 (2006).
34. A. Chakraborty, P.S. Devi, S. Roy, and H.S. Maiti: Low-temperature synthesis of ultrafine $La_{0.84}Sr_{0.16}MnO_3$ powder by an autoignition process. *J. Mater. Res.* **9**(4), 986 (1994).
35. M. Gaudon, C. Laberty-Robert, F. Ansart, P. Stevens, and A. Rousset: Preparation and characterization of $La_{1-x}Sr_xMnO_{3+d}$ ($0 < x < 0.6$) powder by sol–gel processing. *Solid State Sci.* **4**(1), 125 (2002).
36. H. Kuramochi, T. Uzumaki, M. Yasutake, A. Tanaka, H. Akinaga, and H. Yokoyama: A magnetic force microscope using CoFe-coated carbon nanotube probes. *Nanotechnology* **16**(1), 24 (2005).
37. J.E. Lennard-Jones: Cohesion. *Proc. Phys. Soc.* **43**(5), 461 (1931).